

## High- and Low- $\alpha$ Disk Stars Separate Dynamically at all Ages

SUROOR S GANDHI<sup>1</sup> AND MELISSA K NESS<sup>2,3</sup>

<sup>1</sup>*Department of Physics, New York University, 726 Broadway, New York, NY, 10003, USA*

<sup>2</sup>*Center for Computational Astrophysics, Flatiron Institute, 162 5th Ave., New York, NY 10010, USA*

<sup>3</sup>*Department of Astronomy, Columbia University, 550 W 120th St, New York, NY 10027, USA*

### ABSTRACT

There is a dichotomy in the Milky Way in the  $[\alpha/\text{Fe}]$ - $[\text{Fe}/\text{H}]$  plane, in which stars fall into high- $\alpha$ , and low- $\alpha$  sequences. The high- $\alpha$  sequence comprises mostly old stars, and the low- $\alpha$  sequence comprises primarily young stars. The origin of this dichotomy is uncertain. To better understand how the high- and low- $\alpha$ -stars are affiliated, we examine if the high- and low- $\alpha$  sequences have distinct orbits at all ages, or if age sets the orbital properties of stars irrespective of their  $\alpha$ -enhancement. Orbital actions  $J_R$ ,  $J_z$ , and  $J_\phi$  (or  $L_z$ ) are our labels of stellar dynamics. We use ages for 58,278 LAMOST stars (measured to a precision of 40%) within  $\leq 2\text{kpc}$  of the Sun and we calculate orbital actions from proper motions and parallaxes given by Gaia’s DR2. We find that *at all ages*, the high- and low- $\alpha$  sequences are dynamically distinct. This implies separate formation and evolutionary histories for the two sequences; a star’s membership in the high- or low- $\alpha$  sequence indicates its dynamical properties at a given time. We use action space to make an efficient selection of halo stars and subsequently report a group of old, low- $\alpha$  stars in the halo, which may be a discrete population from an infall event.

*Keywords:* stars, Galaxy, Galaxy formation, chemical abundance

### 1. INTRODUCTION

A growing number of extensive stellar surveys including GALAH (De Silva et al. 2015), LAMOST (Cui et al. 2012; Luo et al. 2016), APOGEE (Majewski et al. 2017), RAVE (Kunder et al. 2017; Casey et al. 2017), and Gaia (Gilmore et al. 2012; Gaia Collaboration et al. 2018) are cataloging larger regions of our Galaxy. Subsequently, understanding the structure and formation of the Milky Way is within our reach more than it has ever been before. Each part of the Milky Way (the bulge, disk, and halo) has stars which have different chemical and dynamical properties, as well as possibly different birth properties. Deducing the formation histories of various parts of the Milky Way by studying the chemistry, dynamics and ages of stars in different regions can lead us to understand epochs in the life of the Galaxy itself (e.g. Silva Aguirre et al. 2018). The disk of the Milky Way is the most expansive stellar component, where most of the stellar mass resides, and potentially holds immense

information, which can shed light on how the universe evolves on galactic and cosmological scales.

Disk stars in the Milky Way appear to fall into two broad categories of chemical composition: (1)  $\alpha$ -enhanced or high- $\alpha$  stars, and (2)  $\alpha$ -poor or low- $\alpha$  stars (Fuhrmann 1998; Gratton et al. 2000; Prochaska et al. 2000; Bensby et al. 2003; Venn et al. 2004; Bensby et al. 2005; Adibekyan et al. 2011; Bensby et al. 2014; Anders et al. 2014; Nidever et al. 2014; Hayden et al. 2015). The  $\alpha$ -abundance measurement is typically derived from some ratio of elements fused in Helium capture (i.e. Mg, Si, Ti, Ca). The bimodality seen in the  $[\text{Fe}/\text{H}]$ - $[\alpha/\text{Fe}]$  plane has been inferred to be the signature of two distinct populations (e.g. Mackereth et al. 2018a; Clarke et al. 2019), and chemical enrichment models suggest this requires a mix of populations with distinct enrichment histories (e.g. Nidever et al. 2015). Spectroscopic surveys have established correlations between  $\alpha$ -enhancement and properties such as age (Wyse & Gilmore 1988; Haywood et al. 2013; Bensby et al. 2014; Bergemann et al. 2014): high- $\alpha$  stars are mostly old, and low- $\alpha$  stars are typically young. Quite possibly, the distinct formation timescales and velocity dispersion of the “thin” and “thick” components of the Milky Way disk could translate into  $\alpha$ -abundance signatures. How-

ever, the  $\alpha$ -enhancement of stars does not directly map to their assignment to the thin or thick disk (Feltzing & Bensby 2008; Schönrich & Binney 2009; Adibekyan et al. 2011; Loebman et al. 2011; Bensby et al. 2014; Silva Aguirre et al. 2018; Bland-Hawthorn et al. 2018). Chemistry is our parameter of Galactic inquisition and we wish to understand how the high- and low- $\alpha$  sequences are distributed dynamically at a given age. We have the expectation that this will enable us to better understand the origin of the dichotomy that is seen in the  $[\alpha/\text{Fe}]$ - $[\text{Fe}/\text{H}]$  plane. That is, if the birth and evolution tracks of the high- and low- $\alpha$  sequences might be discrete or related.

To make any sort of generalizable, empirical statement about how the two  $\alpha$ -sequences separate along other axes, we need access to accurately measured properties for a large sample of stars. Gaia DR2 (Gaia Collaboration et al. 2018) measured positions, distances, and proper motions for  $\sim 1.3$  billion objects in the sky, which makes it possible to study the dynamics of stars with unprecedented accuracy. The Large sky Area Multi-Object Spectroscopic Telescope (LAMOST) Survey (Cui et al. 2012) is one of the most extensive catalogs of low-resolution ( $R \sim 1800$ ) spectroscopic data at present. It is an optical ( $3650 - 9000\text{\AA}$ ) survey, and its second data release (Luo et al. 2016) covered  $\sim 500,000$  red giants. *The Cannon*, developed by Ness et al. (2015), provides a data-driven method to infer information about a large number of stars by channeling and combining data from across various astronomical surveys. It has been a challenge to accurately and precisely measure ages for large samples of bright red giant stars that can be observed to vast distances across the Galaxy. This is because there is little discriminating power in stellar models in this regime. However, using *The Cannon*, Ho et al. (2017) created the largest catalog of age estimates for  $\sim 230,000$  red giants by inferring the masses from  $[\text{C}/\text{M}]$  and  $[\text{N}/\text{M}]$  abundances. Data-driven modeling using the correlations between  $[\text{C}/\text{M}]$ ,  $[\text{N}/\text{M}]$ ,  $[\text{Fe}/\text{H}]$ , and age (from asteroseismic determinations) has given us access to a far larger sample of stars for which we can determine ages (Martig et al. 2016; Masseron et al. 2016; Ness et al. 2016).

Actions provide a powerful description of stellar dynamics because they can encapsulate information to uniquely define an orbit (Trick et al. 2018). We use cylindrical coordinates  $(r, \phi, z)$  for positions of stars and calculate actions using:

$$J_i \equiv \oint_{\text{orbit}} p_i dx_i$$

where  $i = r, \phi, z$ , and  $p_i$  is the conjugate momentum (for a detailed introduction to actions see Sellwood 2014;

Binney & Tremaine 2008). If we approximate the Milky Way’s potential to be axisymmetric and its evolution over time to be slow enough, actions are constants of motion for timescales of the order of several orbits (e.g. Bland-Hawthorn et al. 2018). The three actions,  $J_R$ ,  $J_z$ , and  $J_\phi$  (or angular momentum,  $L_z$ ) separately provide physical interpretations of a star’s orbit. (We will use  $L_z$  instead of  $J_\phi$  in our discussion hereafter.)  $J_R$  indicates the eccentricity of an orbit, or an orbit’s deviation from a circle.  $L_z$  is a direct indicator of the radius of the orbit, and  $J_z$  indicates the maximum vertical distance of an orbit from the Galactic plane.

This paper is organized as follows: in §2, we describe the main properties of our data sample, and explain our process of analysis. In §3, we present our main results, and further analysis of the dynamics of the two  $\alpha$ -sequences as a function of  $[\text{Fe}/\text{H}]$  (§3.2) and spatial selection  $|z|$  (§3.3), as well as a comparison of our results with ages derived from Bayesian inference (§3.4). We discuss our results in §4 and point out the detection a sample of old, low- $\alpha$  stars in the halo which might be part of the Gaia Enceladus (§4.2) (e.g. Helmi et al. 2018; Belokurov et al. 2018), before concluding in §5.

## 2. DATA

We investigate  $\sim 60,000$  red giant stars in the disk ( $\leq 2\text{kpc}$  from the Sun) taken from the LAMOST Survey and use their ages as calculated by Ho et al. (2017) (precise up to 0.2 dex), as well as the proper motion and parallax information acquired from Gaia DR2.

Figure 1a shows the number density distribution of our sample in the  $[\alpha/\text{Fe}]$ - $[\text{Fe}/\text{H}]$  plane. We see that, as expected, there are two collections of stars that emerge clearly in this plane (separated roughly by the black line, which we set to differentiate high- and low- $\alpha$  stars). We denote the high- $\alpha$  stars as those that fall above the black line, and the low- $\alpha$  stars are those that fall below the black line. There are 7,334 high- $\alpha$  stars and 50,944 low- $\alpha$  stars in our sample. On average, for our sample, the high- $\alpha$  sequence has an overall lower metallicity ( $[\text{Fe}/\text{H}]$ ) compared to the low- $\alpha$  sequence. At a metallicity of  $[\text{Fe}/\text{H}] \sim -0.2$ , there is a “knee” in the plot (Figure 1a) after which the disparity in the amount of  $\alpha$ -elements and iron-peak elements goes down, and the high- $\alpha$  and low- $\alpha$  sequences appear to converge (e.g. Hayden et al. 2015).

Figure 1b shows the distribution of our sample of (disk) stars once again in the  $[\alpha/\text{Fe}]$ - $[\text{Fe}/\text{H}]$  plane, but colored by age. It becomes apparent that the mean ages of the two sequences are different, in the sense that high- $\alpha$  stars are typically older than the low- $\alpha$  population. However, there is overlap in the age distribution

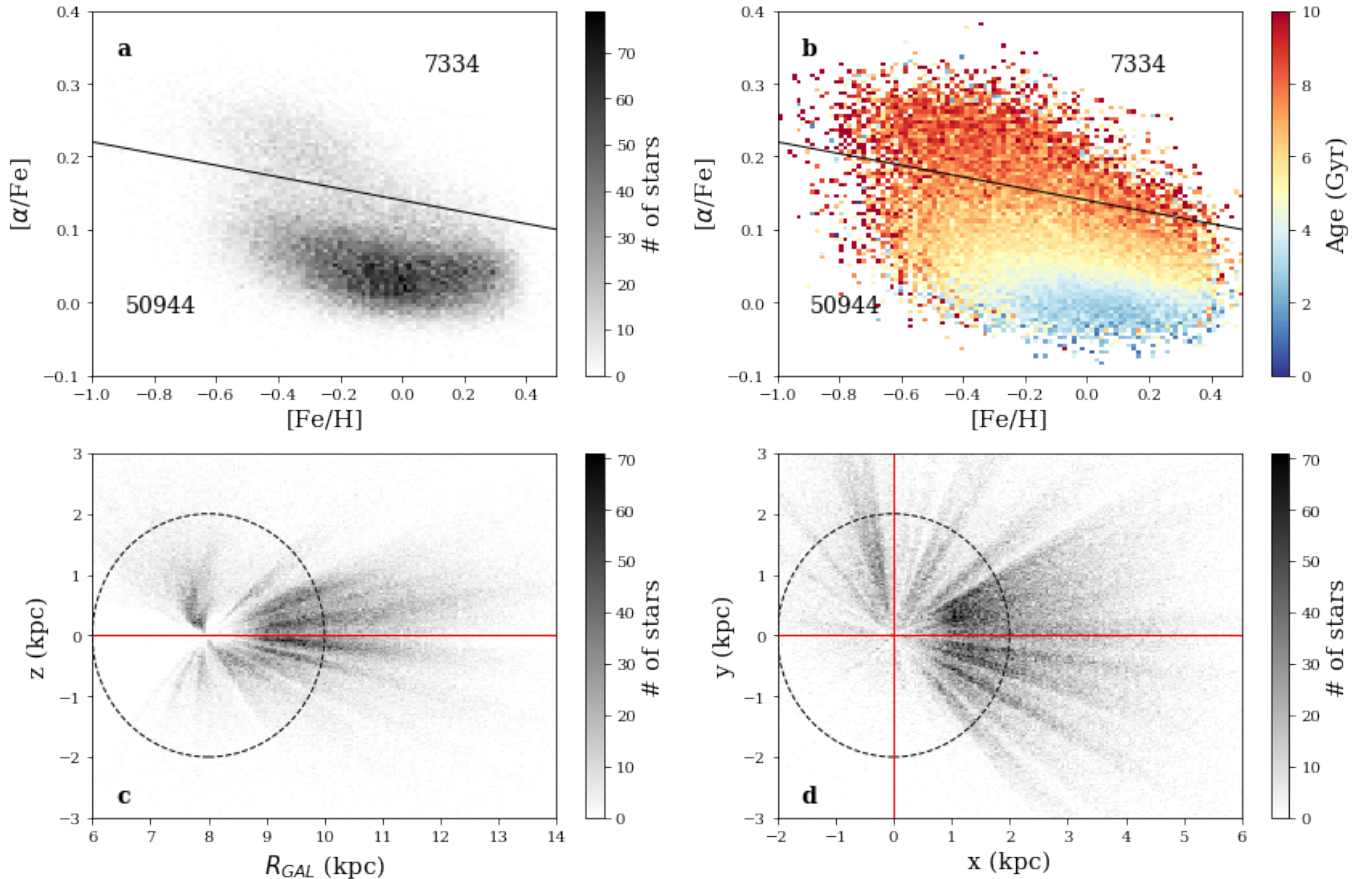


**Figure 1.** Main properties of our data sample of the LAMOST disk red giants. (a) The number density distribution of 58,278 stars is shown in the  $[\alpha/\text{Fe}]$ - $[\text{Fe}/\text{H}]$  plane. We use the black line to differentiate between high- and low- $\alpha$  stars. There are 7,334 high- $\alpha$  stars and 50,944 low- $\alpha$  stars (as indicated in the plot). (b) The same plot as (a), but colored by age. We can see that high- $\alpha$  stars (above the black line) are mostly old, whereas the low- $\alpha$  stars (below the line) are typically much younger. (c) The spatial spread of the  $\sim 150,000$  strong sample is shown in a density plot of  $z$  vs. Galactic radius ( $R_{\text{GAL}}$ ). The Galactic plane at  $z = 0$  is shown by the horizontal red line. Our analyses are restricted to stars within  $\leq 2$  kpc of the Sun, which are encompassed by the dashed circle. (d) The  $x$ - $y$  distribution of stars, again showing our restriction on distance, within the dashed circle of radius  $\leq 2$  kpc. The intersection of the two red lines marks the position of the Sun, at  $R_{\text{GAL}} = 8$  kpc.

and both  $\alpha$ -sequences span stars across a broad range of ages.

Figures 1c,d show the spatial extent of the  $\sim 150,000$  LAMOST stars for which we have age information (from Ho et al. 2017). This full sample extends from a Galactic radius of  $\sim 6$  kpc to  $\sim 14$  kpc, and  $\sim 2$  kpc above and below the Galactic plane. However, we restrict our analysis to disk stars within a distance of  $\leq 2$  kpc of the Sun. This distance cut was implemented because we have used inverse parallax as a proxy for distance, and that estimate becomes erroneous at large distances (Bailer-Jones et al. 2018; Ting & Rix 2018). The spatial extent of stars that we take into account for our study are within the dashed circles in Figures 1c,d.

In Figure 2, the top panel shows normalized distributions of the Galactocentric radius,  $R_{\text{GAL}}$ , for the

high- and low- $\alpha$  sequences, and the lower panel shows the spread of the distance from the Galactic plane,  $z$ , for three different metallicity ranges, (i)  $[\text{Fe}/\text{H}] < -0.5$  (light blue dotted line), (ii)  $-0.5 < [\text{Fe}/\text{H}] < 0$  (aquamarine dashed line), and (iii)  $[\text{Fe}/\text{H}] > 0$  (orange solid line), as explained in the legend in the lower left subplot. (This representation scheme is followed hereafter each time we categorize stars based on  $[\text{Fe}/\text{H}]$ .) The numbers of stars in each metallicity range and  $\alpha$ -sequence is recorded in the bottom subplots in the respective color of the  $[\text{Fe}/\text{H}]$  range. We see a weak gradient in the radii of low- $\alpha$  stars with respect to metallicity; mean  $[\text{Fe}/\text{H}]$  decreases at higher  $R_{\text{GAL}}$  as expected from prior literature which has proposed that the radial metallicity gradient in the Milky Way comes about largely from low- $\alpha$  stars (e.g. Duong et al. 2018).

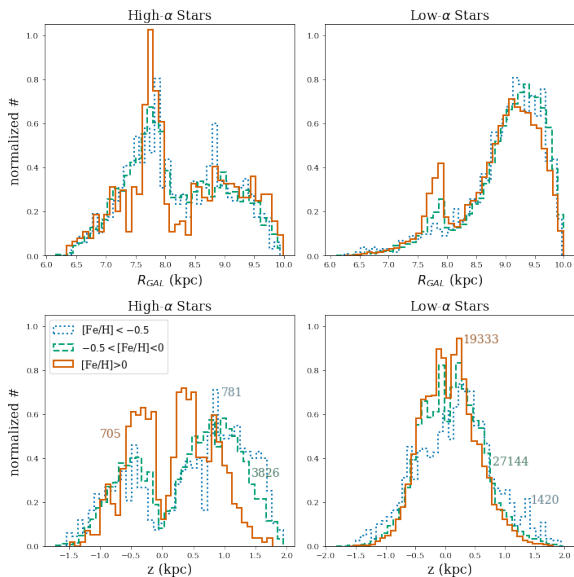


**Figure 2.** Normalized histograms for  $R_{\text{GAL}}$  (top panel) and  $z$  (lower panel) for the two  $\alpha$ -sequences (high- $\alpha$  to the left, low- $\alpha$  to the right) in three different metallicity ranges: (i)  $[\text{Fe}/\text{H}] < -0.5$  (light blue dotted line), (ii)  $-0.5 < [\text{Fe}/\text{H}] < 0$  (aquamarine dashed line), and (iii)  $[\text{Fe}/\text{H}] > 0$  (orange solid line), as explained in the legend in the lower left subplot. The numbers of stars in each metallicity range and  $\alpha$ -sequence is indicated in the lower panels, in the respective color of the  $[\text{Fe}/\text{H}]$  range. We see in the top panel that the two  $\alpha$ -sequences have different mean radii for all metallicity ranges. The low- $\alpha$  stars are preferentially located at larger Galactic radii, compared to the high- $\alpha$  stars. In the lower panel, the dispersion of stars around the mid-plane is clearly much smaller for stars in the low- $\alpha$  sequence compared to the high- $\alpha$  sequence. However, within the high- $\alpha$  sequence, the most metal-rich stars show the narrowest span in  $z$ .

We have stellar ages precise to 0.2 dex from the carbon and nitrogen abundances catalogued in Ho et al. (2017). Additionally, in order to determine precise actions, we need precise and accurate distance measurements (e.g. Coronado et al. 2018; Trick et al. 2018; Beane et al. 2018). We use the inverse of parallax ( $\omega^{-1}$ ) as a proxy for distance and restrict our sample to stars which have a parallax error ( $\delta\omega/\omega$ ) of less than 20%.

We calculate actions using the same method as Trick et al. (2018): by first converting the observable positions and velocities into cartesian ( $X, Y, Z$ ) and heliocentric ( $U_{\text{HC}}, V_{\text{HC}}, W_{\text{HC}}$ ) coordinates, and finally to galactocentric ( $R, \phi, z, v_R, v_T, v_z$ ) coordinates using the `galpy` package (Bovy 2015).  $U$  is the velocity component towards the Galactic center,  $V$  is the component in the direction of rotation of the Galaxy, and  $W$  is the component towards the Galactic north pole. The coordinate conversion from cartesian and heliocentric to galactocentric is necessary to calculate the actions  $J_R$ ,

$J_z$ , and  $L_z$  in `galpy` and is done using  $(U_{\odot}, V_{\odot}, W_{\odot}) = (11.1, 12.24, 7.25) \text{ km s}^{-1}$  as the Sun’s velocity in the Local Standard of Rest (LSR) (Schönrich et al. 2010) and  $(R_{\odot}, \phi_{\odot}, z_{\odot}) = (8, 0, 0.025)$  (with  $R_{\odot}, z_{\odot}$  in kpc) as the Sun’s position within the Galaxy (Jurić et al. 2008).

### 3. RESULTS

#### 3.1. Dynamical Actions as a Function of Age

We examine the actions  $J_R, J_z$ , and  $L_z$  for for 7,334 high- $\alpha$  stars and 50,944 low- $\alpha$  stars as a function of stellar age, and find that the high- and low- $\alpha$  stars have very distinct mean dynamical properties. Figure 3 shows the running mean of each of the actions as a function of age for the two  $\alpha$ -sequences (high- $\alpha$  in blue and vertically hatched, low- $\alpha$  in red and diagonally hatched). In this Figure, each  $\alpha$ -sequence displays distinct dynamical behavior in all three orbital parameters: eccentricity ( $J_R$ ), height above the Galactic plane ( $J_z$ ), and radius ( $L_z$ ). Moreover, the distinction in dynamical trends of the high- and low- $\alpha$  stars is present consistently at all ages.

The running means of actions and age were calculated using a bin size of  $N = 600$  stars for both the  $\alpha$ -sequences. The  $1\text{-}\sigma$  standard deviation ( $\sigma$ ) is used to estimate the dispersion in the running means, and the standard errors are calculated as  $\sigma/(\sqrt{N} - 1)$ . There is a difference of almost a factor of 2 between the mean values of  $J_R$  and  $J_z$  for the high- $\alpha$  and low- $\alpha$  stars, with low- $\alpha$  stars having lower orbital eccentricities and lower vertical excursions. The low- $\alpha$  stars on average have  $\sim 1.25$  times larger angular momentum ( $L_z$ ) than the high- $\alpha$  stars. There are slight gradients in the running means with respect to age, which might be affected by the selection function of the LAMOST survey. Since we have not taken the selection function into account, we make no quantitative measure or claims regarding the trend of the dynamics with respect to age for our sample. The dispersion around the running mean is significant and overlapping between the two  $\alpha$ -sequences.

In Table 1 we report the ratio of average dispersion ( $\bar{\sigma}(J_i)$ ) to average action ( $\bar{J}_i$ ) for each of the three actions of the two  $\alpha$ -sequences. These numbers reported only the average values, and they do not take into account the change in variance over time that is seen in  $J_R$  and  $J_z$  of low- $\alpha$  sequence. However, they do give an adequate idea of the relative dispersion in actions for the high- and the low- $\alpha$  stars in our sample.

#### 3.2. Dynamical Actions for the High- and Low- $\alpha$ Sequence as a Function of $[\text{Fe}/\text{H}]$

We now analyze the two  $\alpha$ -sequences as a function of  $[\text{Fe}/\text{H}]$  to examine if they also separate dynamical

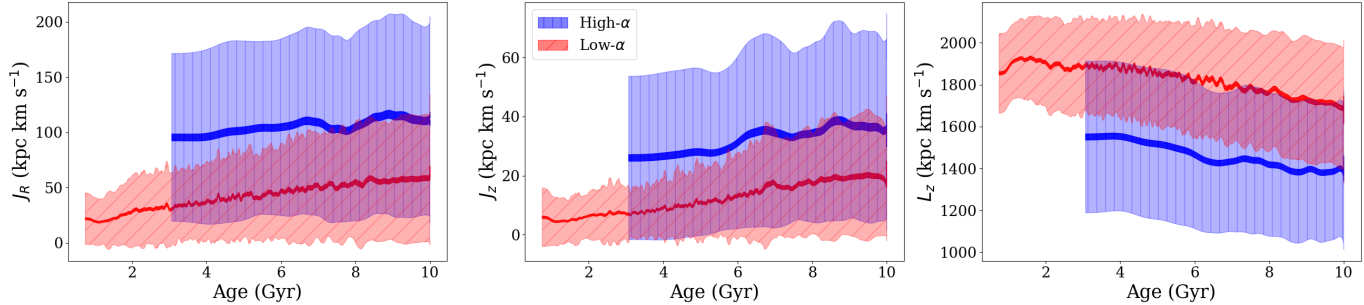


**Figure 3.** Key results of our work. They show that high- and low- $\alpha$  sequences display distinct dynamical trends at all ages, with significant scatter about the mean. The running means (with bin size of  $N = 600$  stars) and standard deviations ( $\sigma$ ) of each of the three actions for 7,334 high- $\alpha$  stars and 50,944 low- $\alpha$  stars are plotted as a function of age. The running means of high- and the low- $\alpha$  sequences are represented by the solid blue curve and the solid red curve respectively. The running means have been smoothed using a Gaussian kernel with  $\sigma_s = 100 \text{ kpc km s}^{-1}$ . The thickness of the solid curves represents the standard error ( $\sigma/\sqrt{N-1}$ ), and the shaded regions are the respective 1- $\sigma$  standard deviation in actions (vertically hatched for high- $\alpha$  and diagonally hatched for low- $\alpha$ ).

Action	$\bar{\sigma}(J_i) / \bar{J}_i$	
	high- $\alpha$	low- $\alpha$
$J_R$	0.79	0.98
$J_z$	0.9	1.13
$L_z$	0.24	0.13

**Table 1.** A table showing the mean 1- $\sigma$  dispersion ( $\bar{\sigma}(J_i)$ ) divided by the mean of each action ( $\bar{J}_i$ ), for the two  $\alpha$ -sequences. The dispersions and running means used in this table are those which are shown in Figure 3.

cally when conditioned on metallicity. Figure 4 shows smoothed running means of  $J_R$ ,  $J_z$ , and  $L_z$  versus age for high- $\alpha$  stars in the left panel, and the low- $\alpha$  stars in the right panel, for three different metallicity ranges of (i)  $[\text{Fe}/\text{H}] < -0.5$ , (ii)  $-0.5 < [\text{Fe}/\text{H}] < 0$ , and (iii)  $[\text{Fe}/\text{H}] > 0$ . The different  $[\text{Fe}/\text{H}]$  ranges are shown with different colors and line styles, as used in Figure 2 and indicated in the legend. The standard errors on these curves are shown by the shaded regions. From these plots, it is quite clear that the mean eccentricity, vertical excursion from the Galactic plane, and angular momentum of the two  $\alpha$ -sequences are distinct even if they have the same metallicity. This Figure also shows the richness of the information linking orbits to stellar chemistry. The high- $\alpha$  stars separate out significantly in  $J_R$  compared to the low- $\alpha$  stars as a function of  $[\text{Fe}/\text{H}]$ , with the lowest metallicity stars showing the highest radial actions. Similarly the high- $\alpha$  stars separate out more markedly, particularly at high metallicity, in  $J_z$  compared to the low- $\alpha$  stars, as a function of  $[\text{Fe}/\text{H}]$ , with the lowest metallicity stars showing the highest vertical actions. The two sequences are similarly dispersed in angular momentum ( $L_z$ ) as a function of  $[\text{Fe}/\text{H}]$ .

This examination demonstrates that there is clearly a relationship between stellar orbits and  $[\text{Fe}/\text{H}]$  that is determined by a star's membership in either the low and high- $\alpha$  sequences. While the stars separate dynamically for these two sequences, the metallicity of a star is additionally indicative of its dynamics at a given age, particularly for the high- $\alpha$  sequence.

### 3.3. Dynamical Actions of the High- and Low- $\alpha$ Sequences as a Function of Spatial Selection, $|z|$

The measured actions are a function of spatial position of the stars; stars at higher distances from the plane in the disk have higher  $J_z$  values and the high- $\alpha$  sequence is preferentially distributed at larger  $|z|$ , at the Sun. We therefore wish to examine in more detail the differences in the action distributions of the high- and low- $\alpha$  sequences conditioned on height from the plane ( $|z|$ ). We examine this by testing the respective actions of the high- and low- $\alpha$  sequences in three narrow slices in  $|z|$ : (i)  $0 < |z| \leq 0.5 \text{ kpc}$ , (ii)  $0.5 < |z| \leq 1 \text{ kpc}$ , and (iii)  $1 < |z| \leq 1.5 \text{ kpc}$ . We find that at the same height from the Galactic plane, the two  $\alpha$ -sequences have mean actions that are different from each other at all ages, as shown in Figure 5. The standard errors on all curves (not shown in the Figure) are on the order of the thickness of the lines.

It can be seen that the high- $\alpha$  stars have significantly higher eccentricity ( $J_R$ ) at all ages compared to the low- $\alpha$  stars even when the stars have the same  $|z|$ -distances. Angular momentum ( $L_z$ ) as a function of age is much lower for high- $\alpha$  stars compared to the low- $\alpha$  stars (at a given  $|z|$ -distance), with stellar angular momenta decreasing with increasing distance from the Galactic plane. Note that there are small differences in  $J_z$  as a function of age (middle panel of Figure 5) for the two  $\alpha$ -sequences; this indicates that within our bins

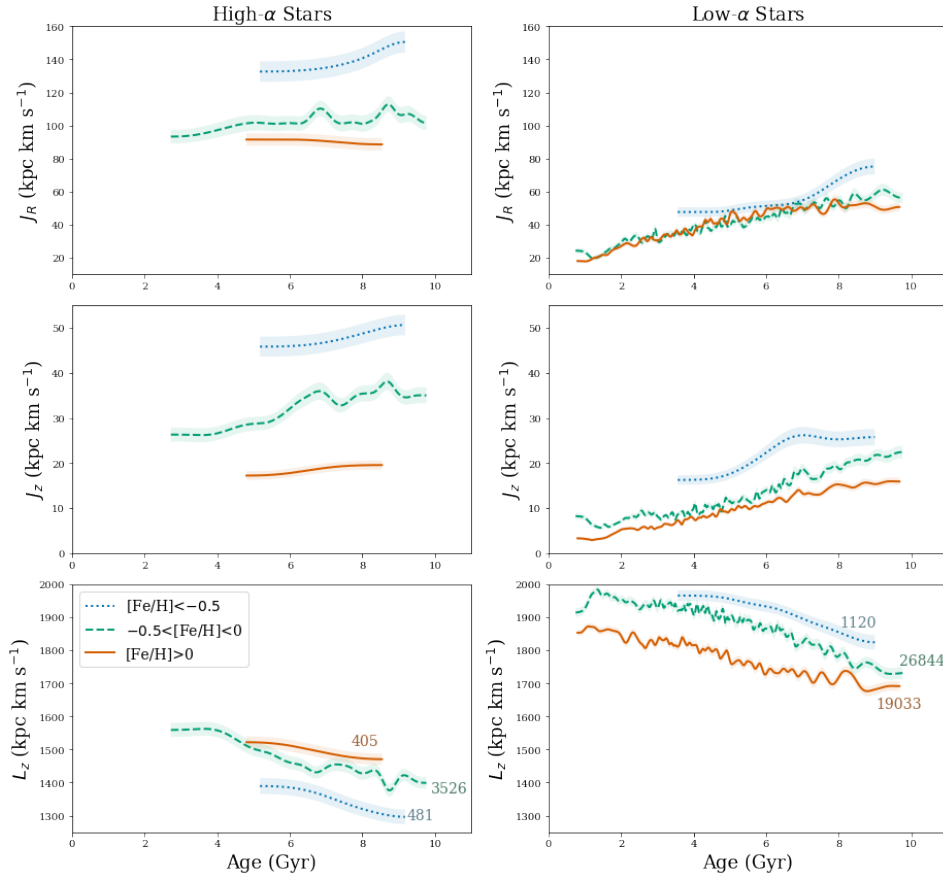


**Figure 4.** Smoothed running means of  $J_R$ ,  $J_z$ , and  $L_z$  (with bin size  $N = 300$ ) for the high- $\alpha$  (left panel) and low- $\alpha$  stars (right panel) as a function of age in three different metallicity ranges. Each  $[\text{Fe}/\text{H}]$  bin is represented by the same color scheme and line style as in Figure 2. The legend for all plots is once again shown in the bottom left subplot, and the number of stars in each  $[\text{Fe}/\text{H}]$  range and  $\alpha$ -sequence is recorded in the bottom panel in the respective color of the  $[\text{Fe}/\text{H}]$  range. We used a gaussian kernel with  $\sigma_s = 100 \text{ kpc km s}^{-1}$  for smoothing the data. The standard errors ( $\sigma/\sqrt{N-1}$ ) are shown by the shaded regions around each curve, which we can see are on the order of the thickness of the lines. These plots make it clear that the two  $\alpha$ -sequences have quite distinct dynamical properties (associated with each of the three actions) at a given metallicity.

of height  $|z|$ , the low- $\alpha$  sequence stars are preferentially nearer to the Galactic plane.

These plots demonstrate that the orbital properties of the stars in each  $\alpha$ -sequence are sensitive to the spatial selection of the stars in height above the plane, which reflects the correlation between structure and chemistry in the Galaxy and also the selection function of the survey. However, it is clear that at a given spatial selection in height above the plane there is the clear separation in the mean of the dynamical action between the two  $\alpha$ -sequences.

### 3.4. Comparison with Ages Derived from Bayesian Inference

We also used ages and actions from a catalog developed by Sanders & Das (2018) to test whether or not we get similar results with their data. In their analysis, Sanders & Das employed Bayesian neural networks to date stars, and the Gaia DR2 data to find the actions us-

ing the Stackel fudge method. Figure 6 shows the plots obtained using the data from Sanders & Das (2018), made in the same way as Figure 3. These plots have 30,579 high- $\alpha$  stars, and 122,668 low- $\alpha$  stars restricted to within  $\leq 2 \text{ kpc}$  of the Sun, and we did a quality cut such that parallax error is  $< 20\%$ . That these data also indicate a distinction in dynamical trends between the two  $\alpha$ -sequences is quite encouraging.

## 4. DISCUSSION

### 4.1. Orbital properties of the High- and Low- $\alpha$ Sequences

Studying the actions  $J_R$ ,  $J_z$ , and  $L_z$  as a function of age for the two  $\alpha$ -sequences makes it clear that disk stars in the solar neighborhood that fall into different  $\alpha$ -enrichment groups have very different mean orbital properties at *all* ages. The fact that this dichotomy in the action plane is present throughout all ages, for all

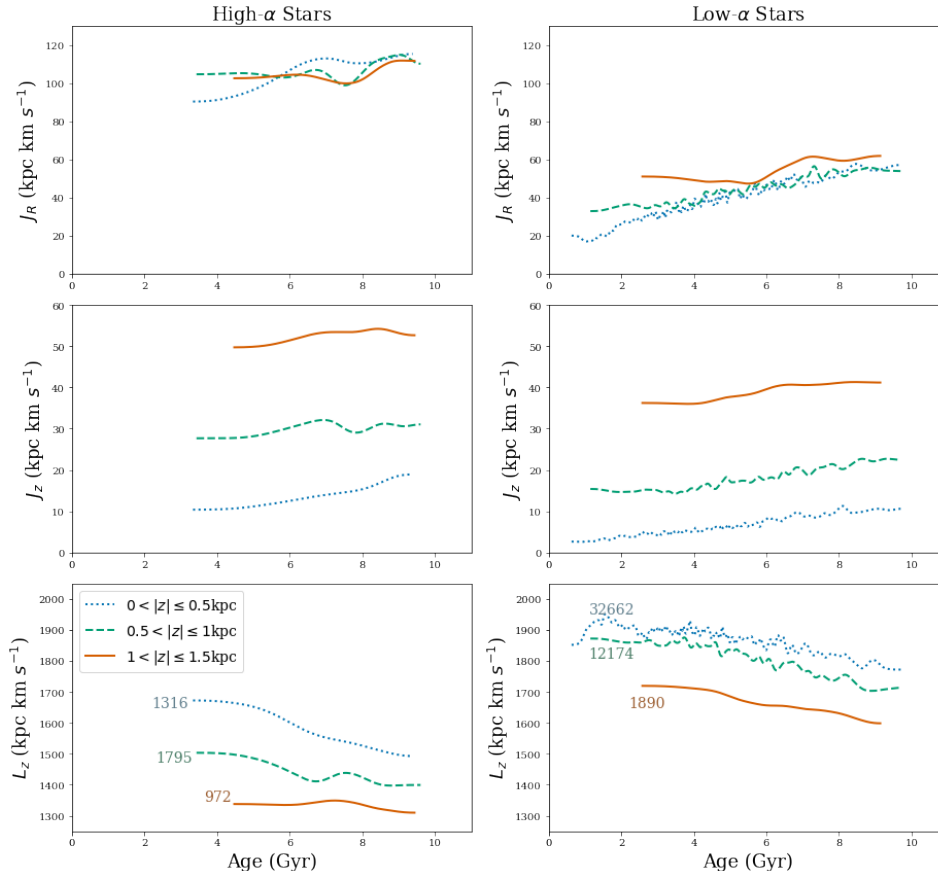


**Figure 5.** Smoothed running means of  $J_R$ ,  $J_z$ , and  $L_z$  versus age for the high- (left panel) and low- $\alpha$  (right panel) sequences separated into three ranges of height above the Galactic plane,  $|z|$ : (i)  $0 < |z| \leq 0.5$  kpc (light blue dotted line), (ii)  $0.5 < |z| \leq 1$  kpc (aquamarine dashed line), and (iii)  $1 < |z| \leq 1.5$  kpc (orange solid line). The legend is shown in the bottom left plot and number of stars in each  $|z|$  range and  $\alpha$ -sequence are recorded in the bottom panel in the respective color of each  $|z|$  range. A gaussian kernel with  $\sigma_s = 100$  kpc km s $^{-1}$  was used for smoothing the running means. Division into  $|z|$  ranges helps decouple the  $|z|$ -positions of the stars from their chemistry and dynamics. We can see that even at the same height from the plane, the two  $\alpha$ -sequences have different  $J_R$ ,  $J_z$ , and  $L_z$ , i.e., different dynamical properties, at all ages. Standard errors have been left out in these plots because they are on the order of the thickness of the curves.

actions, is a strong indication that high- and low- $\alpha$  sequences form distinct populations which have different evolution and birth properties. We also find that within a given  $\alpha$ -sequence, a star’s [Fe/H] is additionally informative as to its orbital properties, particularly for  $J_z$  and  $J_R$  for the high- $\alpha$  sequence. Figure 3 shows our main results, from which we can understand what the nature of the orbits of stars in the high- or low- $\alpha$  sequence is, at least with respect to each other. Orbits of high- $\alpha$  stars are on average more eccentric (have greater  $J_R$ ) than the low- $\alpha$  stars, almost consistently by a factor of two. We see a similar relationship between the two sequences in how much their orbits diverge from the Galactic plane (or  $J_z$ ): the high- $\alpha$  sequence has orbits which go almost up to twice the height from the plane compared to low- $\alpha$  stars. The angular momentum ( $L_z$ ) of low- $\alpha$  stars is  $\sim 1.25$  times that of the high- $\alpha$  stars, which indicates that low- $\alpha$  stars on average have

larger radii than high- $\alpha$  stars (e.g. Beane et al. 2018; Hayden et al. 2015). Our results are consistent with Mackereth et al. (2019), who find similar relationships between  $\alpha$ -abundance and velocity dispersions ( $\sigma_z$ ,  $\sigma_R$ ) of high- and low- $\alpha$  stars. Our findings are also aligned with the analysis of Nidever et al. (2015), who determine single population chemical evolution models to be insufficient to explain the  $\alpha$ -bimodality seen in the APOGEE data. These empirical findings can be explained in a cosmological context if the high- $\alpha$  sequence has a distinct, early and rapid star formation origin, in “clumps” (e.g. Clarke et al. 2019). Such clumps are also observed at high redshift in young spiral Galaxies that are presumably typical Milky Way progenitors (Guo et al. 2015).

It is interesting to note that we find a valley between two slight peaks (in Figure 3) in  $J_R$  and  $J_z$  for the high- $\alpha$  sequence between age  $\sim 6$ -9 Gyr, and a slight peak between two valleys in  $L_z$  for high- $\alpha$  stars in the same age

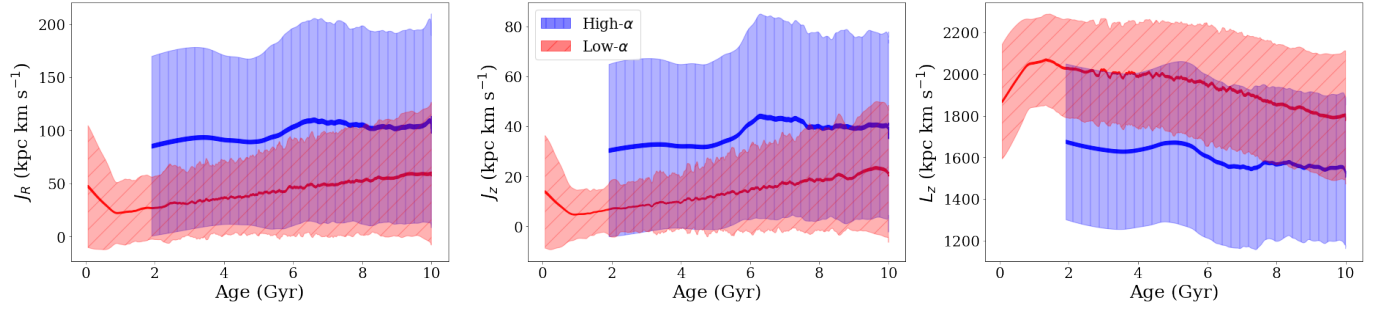


**Figure 6.** The same plots as in Figure 3 but using Sanders & Das (2018) ages and actions. The running means (with bin size  $N = 2000$  stars) and standard deviations ( $\sigma$ ) of each of the three actions for 30,579 high- $\alpha$  stars and 122,668 low- $\alpha$  stars are plotted as a function of age. The high- and the low- $\alpha$  sequences are represented by the solid blue curve and the solid red curve respectively. The running means have been smoothed with a gaussian kernel using  $\sigma_s = 200\text{kpc km s}^{-1}$ . The thickness of the solid curves represents the standard error ( $\sigma/\sqrt{N-1}$ ), and the hatched shaded regions are the respective 1- $\sigma$  standard deviations in actions. These plots quite closely match Figure 3.

window. We see similar signatures in analyzing LAMOST stars from Sanders & Das (2018), as can be seen in Figure 6. The presence of a perturbation in  $J_z$  was also suggested by Beane et al. (2018) (§3.2) for stars in the APOKASC2 sample (independent of  $\alpha$ -enrichment). Such a perturbation could be a signature of an infall event in the Milky Way, which altered the dynamical properties of stars at  $\sim 6$  Gyr. For a bump in actions rather than a net step increase, such an infall would likely trigger the formation of new stars (e.g., a gas cloud merger), as opposed to a merger with a star cluster which would bring in pre-existing stars.

We note that these “bumps” are localized in  $\alpha$ -enrichment as well as metallicity, which means that any infalling gas cloud would have a consistent average chemical composition. As can be seen in Figure 4, they appear only in the high- $\alpha$  sequence in the range of  $-0.5 < [\text{Fe}/\text{H}] < 0$ , within the same age range ( $\sim 6$ -9 Gyr). This leads us to predict that we might expect differences in the detailed elemental composition of this possibly foreign population compared to other high- $\alpha$  stars in the Galaxy of this age.

#### 4.2. Discovery of Old and $\alpha$ -Poor Halo Stars in the LAMOST Sample

Numerous works (e.g. Silva Aguirre et al. 2018; Ness et al. 2016; Bensby et al. 2014; Bergemann et al. 2014; Haywood et al. 2013; Adibekyan et al. 2011) have established that high- $\alpha$  stars of the disk are old and low- $\alpha$  stars of the disk are typically young. Furthermore, Milky Way halo stars ( $\sim 3$ -5kpc from the Sun) are typically high- $\alpha$ , metal poor ( $[\text{Fe}/\text{H}] < -1.0$ ), and old (e.g. Freudenburg et al. (2017); Bovy et al. (2012); Lee et al. (2011); Prochaska et al. (2000); Fuhrmann (1998)). We now examine the  $\alpha$ -sequences for the halo stars in LAMOST including stars within  $\leq 5\text{kpc}$  of the Sun.

To select halo stars in our sample, we take stars that have high radial eccentricities ( $J_R$ ) and low angular momenta ( $L_z$ ). Figure 7a shows how the LAMOST stars are distributed across the  $L_z$ - $\log_{10}(J_R)$  plane; the disk flares out and appears joined to the halo which is distributed around an  $L_z \sim 0$  and high  $J_z$ , as indicated in the box drawn around this region. Such a selection in actions discriminates halo stars from the disk population. This discrete cut is not intended as an absolute marker of halo membership but these stars have orbital properties which align with halo membership and are quite distinct from the disk (e.g. Helmi et al. 2018).

We now show the distribution of our selected halo stars in Figures 7b,c coloured by age and angular momentum, respectively. We use the same line as previously to differentiate high- and low- $\alpha$  stars. Surprisingly, we find low- $\alpha$  stars in the halo in our sample. There are 292 high- $\alpha$  stars and 58 low- $\alpha$  stars which make the halo cut. Respectively, the age distribution of the high- and low- $\alpha$  sequences is similar, with a mean age and 1- $\sigma$  standard deviation of (7.8,2.3)Gyr for the high- $\alpha$  halo stars and (7.2,2.5)Gyr for the low- $\alpha$  stars. These ages may be badly measured, but we found no indication of this in examining the  $\chi^2$  ( $\overline{\chi^2} \sim 0.5$ ) and age uncertainties ( $\overline{\Delta_{age}} \sim 2.2\text{Gyr}$ ) on these stars.

Out of the 58 low- $\alpha$  halo stars, 21 exhibit retrograde motion with  $L_z < 0$ . The metallicity distribution of mean  $[\text{Fe}/\text{H}]$  and the standard error of the mean ( $\sigma_{err} = \sigma/\sqrt{N-1}$ ) is different for the retrograde compared to the prograde low- $\alpha$  stars. The retrograde stars have  $(\overline{[\text{Fe}/\text{H}]} \pm \sigma_{err}) = (-0.70 \pm 0.08)$ , whereas it is  $(-0.45 \pm 0.04)$  for the prograde stars. The retrograde stars are also younger (than the prograde stars) with  $(\overline{age} \pm \sigma_{err}) = (6.23 \pm 0.59)\text{Gyr}$ , whereas for the prograde stars it is  $(7.75 \pm 0.39)\text{Gyr}$ .

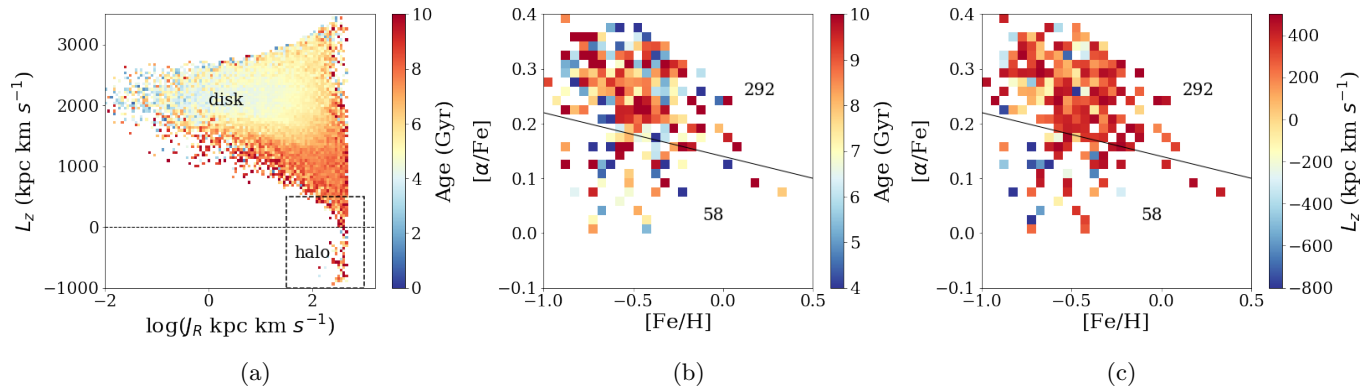


**Figure 7.** (a) The distribution of 144, 231 high- and low- $\alpha$  stars within  $\leq 5$  kpc from the Sun in the  $L_z$ - $\log_{10}(J_R)$  plane, colored by age. The  $L_z$ - $\log_{10}(J_R)$  plane visually separates the disk and the halo; stellar orbits with a variety of angular momenta ( $L_z$ ) and eccentricity ( $J_R$ ) values represent the disk, resulting in the triangular shape of the distribution, whereas the tapering bottom end of the distribution with low  $L_z$  and high  $J_R$  characterizes the halo orbits. In the adjacent plots, we examine the  $\alpha$ -enhancement, age, and orbital motion of halo stars (within the dashed box) with  $\log_{10}(J_R) > 1.5$  and  $L_z < 500$  kpc km s<sup>-1</sup>. (b) The distribution of 350 stars within 5 kpc of the Sun with  $L_z < 500$  kpc km s<sup>-1</sup> and  $\log_{10}(J_R) > 1.5$  are shown in the  $[\alpha/\text{Fe}]$ - $[\text{Fe}/\text{H}]$  plane, colored by age. The numbers of high- and low- $\alpha$  stars are indicated above and below the black separation line respectively. We find that the 58 low- $\alpha$  stars that make this cut have a mean age of  $\sim 7.2$  Gyr, with a  $1\text{-}\sigma$  standard deviation of  $\sim 2.5$  Gyr, whereas the 292 high- $\alpha$  stars which make this cut have a mean age of  $\sim 7.8$  Gyr with a  $1\text{-}\sigma$  standard deviation of  $\sim 2.3$  Gyr. (c) The same as (b), but colored by angular momentum ( $L_z$ ). Of the 58 low- $\alpha$  stars, 21 exhibit retrograde motion, i.e., have  $L_z < 0$ .

This anomalous low- $\alpha$  halo population may be associated with the coherent population of infall discovered in the Gaia data by a number of groups (Myeong et al. 2018; Koppelman et al. 2018; Helmi et al. 2018). In particular, Helmi et al. (2018) find a retrograde population in the halo within 5 kpc of the Sun which they call the ‘‘Gaia Enceladus’’ and show that it might have merged with the Milky Way  $\sim 10$  Gyr ago. At  $[\text{Fe}/\text{H}] \sim -0.6$ , the Gaia Enceladus was demonstrated to be photometrically consistent with an age range of  $\sim 10$ -13 Gyr (Helmi et al. 2018). This infall includes low- $\alpha$  stars as demonstrated using the APOGEE data in Helmi et al. (2018), however has not been previously spectroscopically age dated.

If the stars in the LAMOST data that we have identified as potential Gaia Enceladus members are ex-situ to the Milky Way, they will have experienced a different star formation rate and therefore have different birth and evolution history from the typical stars in the Milky Way. So we expect multiple abundances to show anomalous trends in other elements, which can be tested using individual abundance derivations from LAMOST data (Belokurov et al. 2018; Ting et al. 2017). Additional dimensions of information along these lines will enable us to determine if these stars are from a single or multiple set of infall events.

## 5. CONCLUSION

We calculated actions ( $J_R$ ,  $J_z$ , and  $L_z$ ) using dynamical information from Gaia DR2, and used ages for LAM-

OST red giants (in the disk near the Sun) from Ho et al. (2017). We have found clear indications that  $\alpha$ -enrichment is correlated with dynamical properties of stellar orbits. Our main conclusions are summarized below:

1. Consistently and at all ages, the high- and low- $\alpha$  sequences exhibit distinct mean trends in eccentricity ( $J_R$ ), divergence from Galactic plane ( $J_z$ ), and angular momentum ( $L_z$ )—the three dynamical properties which (simplistically, but uniquely) characterize a stellar orbit. This result can be seen clearly in Figure 3. This implies that the two  $\alpha$ -sequences are distinct populations in the Milky Way, with different birth and evolution properties. This conclusion is also supported by studies which use models to simulate Milky Way-like galaxies and find that the two  $\alpha$ -sequences emerge via distinct birth and evolutionary tracks (e.g. Mackereth et al. 2018b; Grand et al. 2018).
2. The conclusion that chemistry is strongly linked to orbital properties of stars at all ages has been shown to be consistent at a given metallicity (Figure 4) as well as at a narrow slice in height from the plane (Figure 5).
3. The  $L_z$ - $\log_{10}(J_R)$  plane is an effective space to select for halo stars. We find a population of low- $\alpha$  stars which are atypically older and live predominantly in the halo, which may be remnants of

merger events in the Milky Way, e.g. Gaia Enceladus (Helmi et al. 2018; Belokurov et al. 2018).

Our findings of high- and low- $\alpha$  sequences being dynamically distinct at all ages, including at a given ( $[\text{Fe}/\text{H}]$ ,  $|z|$ ) is strong evidence for the discrete origin of these populations in building the disk. These findings are consistent at different spatial locations and for different stellar surveys with different selection functions (e.g. APOGEE (Mackereth et al. 2019; Nidever et al. 2014)).

## 6. ACKNOWLEDGEMENTS

We would like to thank the Flatiron Institute and Columbia University for providing the infrastructure and support for this research. We also thank Glennys Farrar, Angus Beane, and David Hogg for helpful conversations.

## REFERENCES

- Adibekyan, V. Z., Santos, N. C., Sousa, S. G., & Israelian, G. 2011, *A&A*, 535, L11
- Anders, F., Chiappini, C., Santiago, B. X., et al. 2014, *A&A*, 564, A115
- Bailer-Jones, C. A. L., Rybizki, J., Fouesneau, M., Mantelet, G., & Andrae, R. 2018, *AJ*, 156, 58
- Beane, A., Ness, M., & Bedell, M. 2018, *ArXiv e-prints*, arXiv:1807.05986
- Belokurov, V., Erkal, D., Evans, N. W., Koposov, S. E., & Deason, A. J. 2018, *MNRAS*, 478, 611
- Bensby, T., Feltzing, S., & Lundström, I. 2003, *A&A*, 410, 527
- Bensby, T., Feltzing, S., Lundström, I., & Ilyin, I. 2005, *A&A*, 433, 185
- Bensby, T., Feltzing, S., & Oey, M. S. 2014, *A&A*, 562, A71
- Bergemann, M., Ruchti, G. R., Serenelli, A., et al. 2014, *A&A*, 565, A89
- Binney, J., & Tremaine, S. 2008, Princeton University Press, Princeton, NJ, 23, 389
- Bland-Hawthorn, J., Sharma, S., Tepper-Garcia, T., et al. 2018, *ArXiv e-prints*, arXiv:1809.02658
- Bovy, J. 2015, *ApJS*, 216, 29
- Bovy, J., Rix, H.-W., & Hogg, D. W. 2012, *The Astrophysical Journal*, 751, 131
- Casey, A. R., Hawkins, K., Hogg, D. W., et al. 2017, *ApJ*, 840, 59
- Clarke, A. J., Debattista, V. P., Nidever, D. L., et al. 2019, *MNRAS*, 484, 3476
- Coronado, J., Rix, H.-W., & Trick, W. H. 2018, *ArXiv e-prints*, arXiv:1804.07760
- Cui, X.-Q., Zhao, Y.-H., Chu, Y.-Q., et al. 2012, *Research in Astronomy and Astrophysics*, 12, 1197
- De Silva, G. M., Freeman, K. C., Bland-Hawthorn, J., et al. 2015, *MNRAS*, 449, 2604
- Duong, L., Freeman, K. C., Asplund, M., et al. 2018, *MNRAS*, 476, 5216
- Feltzing, S., & Bensby, T. 2008, *Physica Scripta Volume T*, 133, 014031
- Freudenburg, J. K. C., Weinberg, D. H., Hayden, M. R., & Holtzman, J. A. 2017, *ApJ*, 849, 17
- Fuhrmann, K. 1998, *A&A*, 338, 161
- Gaia Collaboration, Brown, A. G. A., Vallenari, A., et al. 2018, *A&A*, 616, A1
- Gilmore, G., Randich, S., Asplund, M., et al. 2012, *The Messenger*, 147, 25
- Grand, R. J. J., Bustamante, S., Gómez, F. A., et al. 2018, *MNRAS*, 474, 3629
- Gratton, R. G., Carretta, E., Matteucci, F., & Sneden, C. 2000, *A&A*, 358, 671
- Guo, Y., Ferguson, H. C., Bell, E. F., et al. 2015, *ApJ*, 800, 39
- Hayden, M. R., Bovy, J., Holtzman, J. A., et al. 2015, *ApJ*, 808, 132
- Haywood, M., Di Matteo, P., Lehnert, M. D., Katz, D., & Gómez, A. 2013, *A&A*, 560, A109
- Helmi, A., Babusiaux, C., Koppelman, H. H., et al. 2018, *ArXiv e-prints*, arXiv:1806.06038
- Ho, A. Y. Q., Rix, H.-W., Ness, M. K., et al. 2017, *ApJ*, 841, 40
- Jurić, M., Ivezić, Ž., Brooks, A., et al. 2008, *ApJ*, 673, 864
- Koppelman, H., Helmi, A., & Veljanoski, J. 2018, *ApJL*, 860, L11
- Kunder, A., Kordopatis, G., Steinmetz, M., et al. 2017, *AJ*, 153, 75
- Lee, Y. S., Beers, T. C., An, D., et al. 2011, *ApJ*, 738, 187
- Loebman, S. R., Roškar, R., Debattista, V. P., et al. 2011, *ApJ*, 737, 8
- Luo, A.-L., Zhao, Y.-H., Zhao, G., et al. 2016, *VizieR Online Data Catalog*, 5149
- Mackereth, J. T., Crain, R. A., Schiavon, R. P., et al. 2018a, *MNRAS*, 477, 5072
- . 2018b, *MNRAS*, 477, 5072
- Mackereth, J. T., Bovy, J., Leung, H. W., et al. 2019, *ArXiv e-prints*, arXiv:1901.04502
- Majewski, S. R., Schiavon, R. P., Frinchaboy, P. M., et al. 2017, *AJ*, 154, 94

- Martig, M., Fouesneau, M., Rix, H.-W., et al. 2016, MNRAS, 456, 3655
- Masseron, T., Merle, T., & Hawkins, K. 2016, BACCHUS: Brussels Automatic Code for Characterizing High accuracy Spectra, Astrophysics Source Code Library, , , ascl:1605.004
- Myeong, G. C., Evans, N. W., Belokurov, V., Sanders, J. L., & Koposov, S. E. 2018, ApJL, 856, L26
- Ness, M., Hogg, D. W., Rix, H.-W., Ho, A. Y. Q., & Zasowski, G. 2015, ApJ, 808, 16
- Ness, M., Hogg, D. W., Rix, H.-W., et al. 2016, ApJ, 823, 114
- Nidever, D. L., Bovy, J., Bird, J. C., et al. 2014, ApJ, 796, 38
- Nidever, D. L., Holtzman, J. A., Allende Prieto, C., et al. 2015, AJ, 150, 173
- Prochaska, J. X., Naumov, S. O., Carney, B. W., McWilliam, A., & Wolfe, A. M. 2000, AJ, 120, 2513
- Sanders, J. L., & Das, P. 2018, MNRAS, 481, 4093
- Schönrich, R., & Binney, J. 2009, MNRAS, 399, 1145
- Schönrich, R., Binney, J., & Dehnen, W. 2010, MNRAS, 403, 1829
- Sellwood, J. A. 2014, Reviews of Modern Physics, 86, 1
- Silva Aguirre, V., Bojsen-Hansen, M., Slumstrup, D., et al. 2018, MNRAS, 475, 5487
- Ting, Y.-S., & Rix, H.-W. 2018, arXiv e-prints, arXiv:1808.03278
- Ting, Y.-S., Rix, H.-W., Conroy, C., Ho, A. Y. Q., & Lin, J. 2017, ApJL, 849, L9
- Trick, W. H., Coronado, J., & Rix, H.-W. 2018, ArXiv e-prints, arXiv:1805.03653
- Venn, K. A., Irwin, M., Shetrone, M. D., et al. 2004, AJ, 128, 1177
- Wyse, R. F. G., & Gilmore, G. 1988, AJ, 95, 1404